N92-22537

ADVANCED PROPELLER RESEARCH

John F. Groeneweg
and
Lawrence J. Bober

SUMMARY

Recent results of aerodynamic and acoustic research on both single-rotation and counterrotation propellers are reviewed. Data and analytical results are presented for three propellers: SR-7A, the single-rotation design used in the NASA Propfan Test Assessment (PTA) flight program; CRP-X1, the initial 5+5 Hamilton Standard counterrotating design; and F7-A7, the 8+8 counterrotating General Electric design used in the proof-of-concept Unducted Fan (UDF) engine. In addition to propeller efficiencies, cruise and takeoff noise, and blade pressure data, off-design phenomena involving formation of leading-edge vortexes are described. Aerodynamic and acoustic computational results derived from three-dimensional Euler and acoustic radiation codes are presented. Research on unsteady flows which are particularly important for understanding counterrotation interaction noise, unsteady loading effects on acoustics, and flutter or forced response is described. The first results of three-dimensional unsteady Euler solutions are illustrated for a single-rotation propeller at angle of attack and for a counterrotation propeller. Basic experimental and theoretical results from studies of the unsteady aerodynamics of oscillating cascades are outlined. Finally, advanced concepts involving swirl recovery vanes and ultra-high-bypass ducted propellers are discussed.

INTRODUCTION

This review addresses three aspects of propeller research: analysis, verification of the analysis with experiment, and studies of advanced concepts. Single-rotation and counterrotation sections address cruise performance, noise at both cruise and takeoff, and specific topics such as blade pressure measurements, leading-edge vortexes associated with off-design operation, and results from steady Euler analysis. In the area of unsteady aerodynamics, recent unsteady three-dimensional Euler results are shown together with theoretical and experimental results from work on transonic cascades. A concluding section discusses advanced concepts and the future work emphases required to address them.

Recent wind tunnel tests (refs. 1 to 3) have provided data on the three advanced high-speed propeller models described in table I. The SR-7A model is the most recent in a series of single-rotation designs (ref. 4) and is an aeroelastically scaled model of the 9-ft-diameter Large-Scale Advanced Propeller (LAP) being used in the Propfan Test Assessment (PTA) Flight Program (refs. 5

and 6). The F7-A7 is a scale model of the counterrotation pusher propeller being used on the Unducted Fan (UDF) demonstrator engine (ref. 7). The CRP-X1 model simulates a counterrotation tractor propeller. All three propeller models have a nominal diameter of 2 ft. Note that the F7-A7 has the highest hub-to-tip ratio and cruise loading.

SINGLE-ROTATION TECHNOLOGY

Figure 1 shows the SR-7A installed in the NASA Lewis 8- by 6-Foot Wind Tunnel, where its aerodynamic, acoustic, and aeroelastic performances were measured at cruise conditions. The laser beams are part of a system used to measure mean blade deflections during propeller operation (i.e., the so-called "hot" blade shape).

Net efficiency of the SR-7A propeller model is shown in figure 2, together with results from five earlier models. Detailed design parameters for each of the propellers are listed in table II. Measured net efficiencies are shown in figure 2 as a function of free-stream Mach number, with each propeller's design loading parameter C_p/J^3 kept constant with Mach number. At Mach 0.80, the design point for SR-7A, its efficiency lies on the upper bound of measured efficiencies. The SR-2 propeller has the lowest performance because it is the only one of these models which has no blade sweep.

The peak fundamental tone levels for SR-7A are plotted in figure 3 as a function of helical tip Mach number (ref. 8). Advance ratio is constant at 3.06, and the near-field measurements were made on a sideline parallel with the propeller axis at 0.3 propeller diameter from the propeller tip. Data for three loading levels are shown as indicated by the blade setting angles bracketing the design valve. The striking feature of the tone variation with helical tip Mach number is the behavior in the supersonic range beyond 1.1. The peak fundamental tone levels no longer increase and may peak, level off, or decrease depending on loading. This result indicates that higher cruise and propeller speeds do not necessarily mean increased cabin noise problems.

The SR-7A propeller model was also tested in the NASA Lewis 9- by 15-Foot Anechoic Wind Tunnel to measure far field noise and performance at typical takeoff and approach conditions (Mach 0.2). Figure 4 shows the model installed on a swept wing used to determine installation effects. The entire propeller-wing assembly may be rotated to angle of attack in the horizontal plane. The continuously traversing microphones (at right) measure far field noise corresponding to levels measured below an aircraft during flyover. Fixed microphones on the walls measure noise in the other three directions and are staggered with respect to the tunnel flow to avoid wake interference on downstream microphones. The walls are acoustically treated to provide anechoic conditions down to a frequency of 250 Hz, well below the fundamental frequency for the propeller model.

The effect of angle of attack on the flyover noise of SR-7A without the wing is shown in figure 5 (ref. 9). Fundamental tone directivities are shown for four angles of attack ranging from 0° to 15°. The peak levels, approximately in the plane of rotation, increased by about 10 dB. A typical maximum takeoff angle of the propeller centerline with respect to the aircraft flight path is about 8°; thus takeoff noise would be increased on the order of 5 dB because of unsteady loading at that angle of attack.

A detailed knowledge of propeller blade surface pressures is important for aerodynamic code validation and as input to acoustic calculations. A two-blade version of the eight-blade Large-Scale Advanced Propeller (LAP) was tested in the ONERA S1 wind tunnel to obtain steady and unsteady blade pressures over a wide range of operating conditions (fig. 6). Only two blades were used because of the limited total power available to drive the propeller. In this way the propeller could be operated at a reasonable power per blade. The large size of this propeller (9-ft diam) allowed much more detailed measurements than could be obtained on the 2-ft-diameter models tested previously.

Sample results of the steady blade pressure distributions measured are shown in figure 7 at several spanwise locations on the LAP at a low-speed, high-power condition. The pressure distributions at the two locations nearest the tip lack the high suction peaks of the inboard locations because of the presence of leading-edge and tip vortexes at the outboard locations. Similar data were obtained at 12 additional operating conditions, providing valuable data for code verification.

A schematic of leading-edge and tip vortexes is shown in figure 8, together with curves showing the consequences of using analyses which neglect their presence. When the propeller is operating appreciably off the cruise design point, such as at takeoff, a leading-edge vortex which merges with the tip vortex is expected to form, as shown schematically. The phenomenon is similar to the vortex structure on a delta wing aircraft at high angle of attack. If the associated altered loading distribution is not accounted for in analytical models, errors in aerodynamic performance and the tone noise level predictions will result as illustrated.

In addition to the blade pressure data, flow visualization of propeller blade surface flows at off-design conditions has indicated the presence of leading-edge and tip vortexes (refs. 1 and 10). Fluorescent oil flow patterns on the pressure side of the SR-3 blade at the Mach 0.8, windmill condition are shown in figure 9. Streaks in the oil at the blade surface are influenced by two main factors. Centrifugal forces cause radial flow in the oil film. Shear flow forces at the surface act mainly along streamlines. Over much of the blade the streaks are at an angle determined by these two forces. However, near the leading edge on the outboard portion of the blade and at the tip, the lines are primarily radial. This indicates a different flow regime, interpreted as the existence of a leading-edge vortex merging with a tip vortex.

This flow phenomenon has recently been predicted computationally. An Euler code developed at NASA Lewis (ref. 11) was run at United Technologies Research Center (UTRC) with an order of magnitude increase in grid points to about 200 000. When particle paths were traced they revealed the leading-edge vortex which merges with the tip vortex flow, as shown in figure 10. The operating condition at Mach 0.2 and advance ratio of 1.0 is typical of a takeoff situation which involves high incidence angles. Apparently, numerical "viscosity" is sufficient to trigger vortex formation and produce at least a qualitative description of this flow phenomenon.

COUNTERROTATION TECHNOLOGY

The counterrotation tractor propeller model, designated CRP-X1, was designed and built by Hamilton Standard under contract to NASA Lewis and is shown installed in the UTRC high-speed wind tunnel in figure 11. The front and rear propellers are independently driven by two air-driven turbines. Propeller performance and flow field data, as well as blade stresses, were measured during these tests (ref. 2). Propeller acoustic data were obtained during separate tests in the UTRC Acoustic Research Tunnel (ref. 12).

Figure 12 shows the net efficiency of the CRP-X1 propeller model as a function of power loading at three free-stream Mach numbers. At the design power loading of 37.2 shp/D^2, the data indicate a net efficiency of approximately 85 percent for Mach numbers in the range of 0.7 to 0.8. The efficiency also remains high over a wide range of power loadings. The predicted efficiency agrees very well with the data at Mach 0.8, but somewhat overpredicts the efficiency at the lower Mach numbers.

An example of acoustic data obtained on CRP-X1 (ref. 12) is shown in figure 13. Levels of the first five harmonics of single-rotation (SRP) and counterrotation (CRP) propeller noise are shown at three axial locations in the far field: forward, aft, and in the plane of rotation. The single-rotation fundamental tone levels are adjusted upward 3 dB to compare the equivalent noise of two independent propellers with the CRP-X1 counterrotation configuration. Single-rotation and counterrotation fundamental tones are then roughly equal, but the counterrotation harmonic levels are dramatically higher at all locations due to the unsteady aerodynamic interactions between blade rows. This characteristic of high foreward and aft harmonic levels must be dealt with to achieve acceptable counterrotation community noise levels.

In figure 14 the NASA Lewis counterrotation pusher propeller test rig is shown installed in the 8- by 6-Foot Wind Tunnel. The propeller shown is the F7-A7 configuration described in table I. The tunnel has holes in the walls equivalent to about 6 percent porosity to minimize wall interactions at transonic speeds. The rig is strut mounted and is powered by two turbines using 450-psi drive air. Performance, flow field, and acoustic measurements are made.

Examples of the blade configurations tested are shown in figure 15 and include designs for Mach 0.72 cruise (top row) and Mach 0.8 cruise (bottom row). The designs differed in tip sweep, planform shape, airfoil camber, and a significantly shortened aft rotor (A3). The planform shapes for most forward and aft rotors were very similar. The A21 aft rotor planform is included since it differs so much from the F21 front rotor. The F1-A1 configuration is very similar to F7-A7 but with reduced camber, which is expected to improve cruise efficiency. F1-A3 was run to see the aerodynamic and acoustic effects of a short aft rotor. These blades were designed and built by the General Electric Company, several under contract to NASA Lewis.

Net efficiencies for F7-A7 are shown in figure 16 as a function of Mach number for three loadings: design, 80 percent, and 120 percent of design. Tip speed was held constant at the design value of 780 ft/sec. At the design Mach number of 0.72, efficiency depends quite strongly on loading: increased loading decreases efficiency. At Mach numbers significantly higher than design, compressibility losses dominate, and efficiencies fall off nearly independent of loading.

Counterrotation fundamental tone levels at cruise conditions are shown in figure 17. Fundamental tone directivities for F7-A7, the proof-of-concept UDF configuration, are compared for model data from the NASA Lewis 8- by 6-Foot Wind Tunnel scaled to full-scale cruise conditions, full-scale flight data obtained by the formation flight of the instrumented NASA Lewis Learjet with the UDF engine on the 727, and predicted levels from a frequency domain model developed by General Electric. There is good agreement between the model wind tunnel measurements and full-scale flight data, particularly since the in-flight automation pitch control system did not allow the full-scale aft blade pitch angles to be matched with available model data. Predicted levels agree quite well with the data except for the forward angles.

Noise and performance measurements were also made on counterrotation models at takeoff/approach conditions. In figure 18 the model of the 8+8 configuration of the propeller used on the UDF proof-of-concept engine is shown in the 9- by 15-Foot Anechoic Wind Tunnel, where extensive community noise tests were conducted. Unequal blade numbers, differential diameter, rotor-to-rotor spacing, angle of attack, and effects of an upstream support pylon were investigated. A continuously traversing microphone (not shown) was also used to map the asymmetric sound field with the model at angle of attack or with a pylon installed. The tunnel walls are acoustically treated to make the test section anechoic down to 250 Hz, well below the fundamental tone frequency of the model.

Examples of counterrotation propeller noise at the takeoff conditions are shown in figure 19 (ref. 13). Measured and predicted directivities of the front rotor fundamental and the first interaction tone for F7-A7 at Mach 0.2 are compared. The predictions are from a frequency domain theory developed at General Electric. Note again the high levels of interaction tone noise at both forward and aft angles, in contrast to the forward rotor alone fundamental which peaks in the plane of rotation. Agreement between theory and data is very good for the front rotor fundamental. The predicted shape of the first interaction tone agrees well with the data, but the levels are underpredicted at the extremes in angle, indicating that more code development work is required for the interaction noise sources.

A counterrotation Euler code developed at NASA Lewis (ref. 12) has been used to obtain numerical predictions of the flow about one version of the UDF. The solution is obtained by iterating between the front and rear blade rows. The coupling between rows is done in a circumferentially averaged sense, so there are no blade-wake interactions included. The results in figure 20 show the pressure distribution on the nacelle and blade surfaces as well as on a plane perpendicular to the axis of rotation at the aft end of the nacelle. The flow field pressures were taken from the flow field of the rear row and show near-field acoustic pressure perturbations spiraling out into the flow. The calculations were done at Cray Research, and the flow field was displayed by using the code MOVIE-BYU.

UNSTEADY AERODYNAMICS

Fully unsteady, three-dimensional Euler code solutions have recently been obtained for advanced propeller geometries (ref. 14). Results from the unsteady Euler code solution for the SR-3 propeller with its axis at 4° to the mean 0.8 Mach number flow are shown in figure 21. As the propeller rotates, downward moving blades (on the right in the figure) experience the highest incidence, upward blades (on the left) the lowest, and top and bottom are near the mean. Pressure contours for regions where the absolute flow velocities are supersonic are plotted in alternate blade passages. Large regions of supersonic flow are shown for the high incidence, high loading positions with much smaller supersonic regions corresponding to lower incidences and loadings.

The unsteady Euler solution algorithms were also applied to the 8+8-configuration F7-A7 counterrotation propeller to obtain a full unsteady, three-dimensional solution for the flow field. A sample of the results in the form of pressure contours in a plane just downstream of both blade rows is shown in figure 22 (ref. 14). These contours, which are for a particular instant in time, show a low pressure island structure indicative of the tip vortexes shed by the blades. Current solution methods handle equal blade numbers in each row and are being extended to treat the general case of unequal blade numbers.

An experimental and analytical research program is being conducted to understand the flutter and forced response characteristics of advanced high-speed propellers. A comparison of measured and calculated flutter boundaries for a propfan model, called SR3C-X2, is shown in figure 23 (refs. 15 and 16). The theoretical results from the NASA Lewis-developed ASTROP3 analysis include the effects of centrifugal loads and steady-state, three-dimensional air loads. The analysis does reasonably well in predicting the flutter speeds and slopes of the boundaries. However, the difference between the calculated and measured flutter Mach numbers is greater for four blades than for eight blades. This implies that the theory is overcorrecting for the decrease in the aerodynamic cascade effect with four blades.

Wind tunnel tests of the SR-5 propeller demonstrated that cascade effects and sweep effects have a destabilizing influence on the flutter boundary at relative Mach numbers approximately equal to 1. Experimental research conducted in the NASA Lewis transonic oscillating cascade will investigate the subsonic and transonic steady and unsteady aerodynamics relevant to advanced turboprops. (See fig. 24.) An unswept cascade will provide baseline data. Following that, the aerodynamics of a cascade of airfoils with sweep will be quantified. Both subsonic and transonic flow fields will be investigated as the airfoils undergo torsional oscillations at realistic reduced frequency values.

A compressible, unsteady, full Navier-Stokes, finite-difference code has been developed for modeling transonic flow through two-dimensional, oscillating cascades (ref. 17). The procedure introduces a deforming grid technique to capture the motion of the airfoils, as shown on the left portion of figure 25, which is for an interblade phase angle of 90°. The use of the deforming grid is convenient for treatment of the outer boundary conditions since the outer boundary can be fixed in space, while the inner boundary moves with the blade motion. The code is an extension of the isolated airfoil code developed at the Georgia Institute of Technology (ref. 18). The motion of the shock wave is evident in the chordwise pressure distributions shown at the right in figure 25.

ADVANCED CONCEPTS

The swirl recover vane experiment will investigate the fuel-saving and noise benefits available by adding swirl recovery vanes (SRV) behind a propfan, as shown in figure 26. Thus, the 1000-hp, single-rotation propeller test rig will be modified to accept a new balance and eight swirl recovery vanes. These tests will determine the fuel-saving benefits of the SRV concept over its Mach number operating range (0 to 0.85). Other parametric variations will include vane angle and vane axial spacing relative to the propfan. Design calculations indicate that as much as two-thirds of the efficiency increment available from counterrotation (8 to 10 percent) can be obtained with the swirl recovery vanes.

For long-range aircraft with wing-mounted engines, ducted propellers (ultra-high-bypass fans) have installation advantages in terms of limiting the diameter required for a given thrust. Technical issues associated with these configurations which require research are noted for high-speed cruise in the upper half of figure 27 and for low-speed takeoff or approach in the lower half. At cruise, the drag of the large-diameter thin cowl must be minimized while achieving acceptable near-field sound levels. A synthesis of propeller and fan aerodynamic design methods is required to arrive at an optimum combination of sweep and of axial and tip Mach numbers. At low speed, far-field community noise, cowl-lip separation at high angles of attack with the associated blade stresses, and reverse thrust operation must each be addressed.

CONCLUDING REMARKS

The status of current and future propeller research in each of the three disciplines (aerodynamics, acoustics, and aeroelastics) is summarized in figure 28. Presently, aerodynamic work emphasizes three-dimensional steady Euler solutions and performance measurements with some diagnostics, while future work is moving toward three-dimensional unsteady Euler and Navier-Stokes codes with more emphasis on detailed flow field diagnostics. Acoustically, three-dimensional codes are used with detailed steady aerodynamic input, and extensive cruise and takeoff signatures have been measured for both single rotation and counterrotation. Future efforts will emphasize unsteady aerodynamic inputs to the codes to describe interaction and installation effects, and experiments will concentrate on detailed noise maps for installed configurations. Current aeroelastics focus has been on prediction and measurement of flutter boundaries and constructing the first generation of structural design optimization codes. In the future, flutter boundary measurement and prediction will be extended to counterrotation, and the phenomena of stall flutter and forced response will receive more emphasis. Future emphasis in all three disciplines will involve addressing the technical issues associated with ultra-high-bypass ducted propellers.

REFERENCES

1. Stefko, G.L.; Rose, G.E.; and Podboy, G.G.: Wind Tunnel Performance Results of an Aeroelastically Scaled 2/9 Model of the PTA Flight Test Prop-Fan. AIAA Paper-87-1893, June 1987 (NASA TM-89917).

2. Wainauski, H.S.; and Vaczy, C.M.: Aerodynamic Performance of a Counter Rotating Prop-Fan. AIAA Paper 86-1550, June 1986.

3. Sullivan, T.J.: Aerodynamic Performance of a Scale-Model, Counter-Rotating Unducted Fan. Advanced Technology for Aero Gas Turbine Components, AGARD CP-421, AGARD, Neuilly-Sur-Seine, France, 1987, pp. 22-1 to 22-16. (Avail. NTIS, AD-A198664.)

4. Mikkelson, D.C.; Mitchell, G.A.; and Bober, L.J.: Summary of Recent NASA Propeller Research. AGARD Conference Paper, Oct. 1984 (NASA TM-83733).

5. Whitlow, J.B., Jr.; and Sievers, G.K.: Fuel Savings Potential of the NASA Advanced Turboprop Program. NASA TM-83736, 1984.

6. Graber, E.J.: Overview of NASA PTA Propfan Flight Test Program. Aeropropulsion '87, NASA CP-10003, 1987.

7. Stuart, A.R.: The Unducted Fan Engine. AIAA Paper 85-1190, July 1985.

8. Dittmar, J.H.; and Stang, D.B.: Cruise Noise of the 2/9 Scale Model of the Large-Scale Advanced Propfan (LAP) Propeller, SR-7A. AIAA Paper 87-2717, Oct. 1987 (NASA TM-100175).

9. Woodward, R.P.: Measured Noise of a Scale Model High Speed Propeller at Simulated Takeoff/Approach Conditions. AIAA Paper 87-0526, Jan. 1987.

10. Vaczy, C.M.; and McCormick, D.C.: A Study of the Leading Edge Vortex and Tip Vortex on Propfan Blades. J. Turbomachinery, vol. 109, no. 3, July 1987, pp. 325-331.

11. Celestina, M.L.; Mulac, R.A.; and Adamczyk, J.J.: A Numerical Simulation of the Inviscid Flow Through a Counter-Rotating Propeller. NASA TM-87200, 1986.

12. Magliozzi, B.: Noise Characteristics of a Model Counter-Rotating Propfans. AIAA Paper 87-2656, Oct. 1987.

13. Woodward, R.P.: Noise of a Model High Speed Counterrotation Propeller at Simulated Takeoff/Approach Conditions (F7/A7). AIAA Paper 87-2657, Oct. 1987 (NASA TM-100206).

14. Whitfield, D.L., et al.: Three-Dimensional Unsteady Euler Solution for Propfans and Counter-Rotating Propfans in Transonic Flow. AIAA Paper 87-1197, June 1987.

15. Kaza, K.R.V., et al.: Analytic Flutter Investigation of a Composite 14. Kaza, Propfan Model. NASA TM-88944, 1987.

16. Ernst, M.A.; and Kiraly, L.J.: Determining Structural Performance. Aeropropulsion '87, NASA CP-10003, 1987.

17. Huff, D.L.: Numerical Simulations of Unsteady, Viscous, Transonic Flow Over Isolated and Cascade Airfoils Using a Deforming Grid. AIAA Paper 87-1316, June 1987 (NASA TM-89890).

18. Sankar, N.L.; and Tang, W.: Numerical Solution of Unsteady Viscous Flow Past Rotor Sections. AIAA Paper 85-0129, Jan. 1985.

TABLE I. - ADVANCED PROPELLER DESIGN PARAMETERS

Design	Number of blades	Radius ratio	Cruise Mach number	Cruise loading, shp/D^2	Tip speed, ft/sec
SR-7	8	0.24	0.80	32.0	800
F7-A7	8+8	.425	.72	55.5	780
CRP-X1	5+5	.240	.72	37.2	750
		.275	.72	37.2	750

TABLE II. - SINGLE-ROTATION PROPELLER DESIGN PARAMETERS

Design	Number of blades	Sweep angle, deg	Power coefficient, C_p	Advance ratio, J	Loading parameter, C_p/J^3	Tip speed, ft/sec
SR-7A	8	41	1.45	3.06	0.0509	800
SR-6	10	40	2.03	3.50	.0474	700
SR-3	8	45	1.70	3.06	.0593	800
SR-1M	8	30	1.70	3.06	.0593	800
SR-2	8	0	1.70	3.06	.0593	800

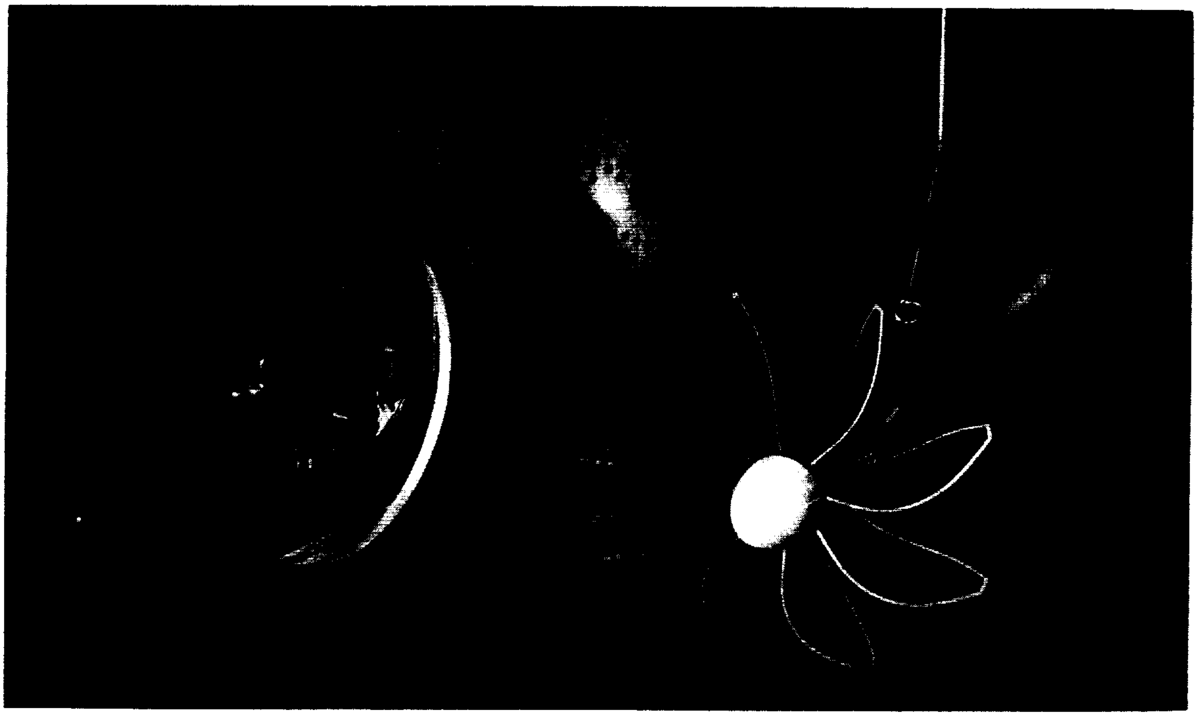

CD-87-29482

Figure 1. - SR-7A propeller in Lewis 8- by 6-Foot Wind Tunnel.

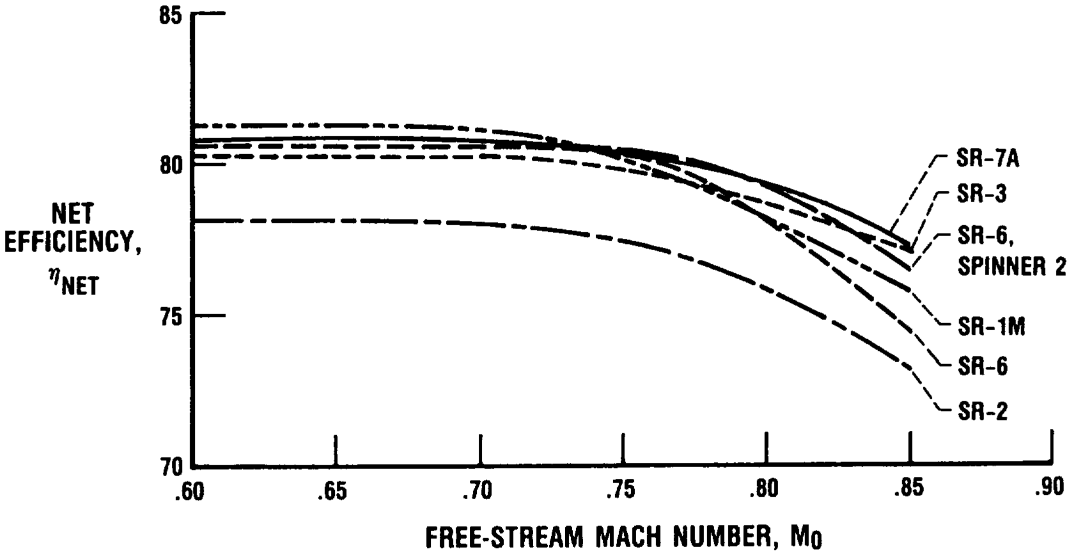

CD-87-29483

Figure 2. - Single-rotation propeller performance.

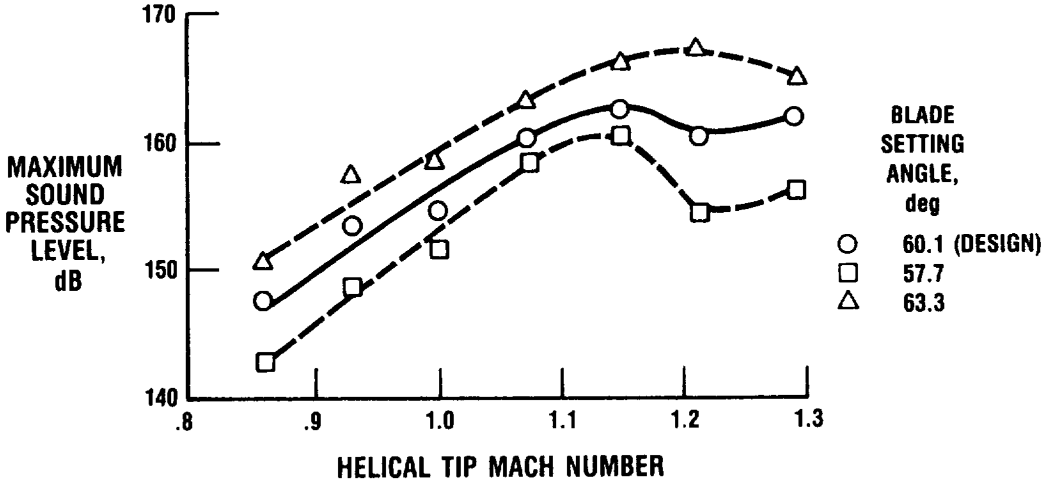

CD-87-29484

Figure 3. - SR-7 peak blade passing tone variation with helical tip Mach number (constant advance ratio, 3.06).

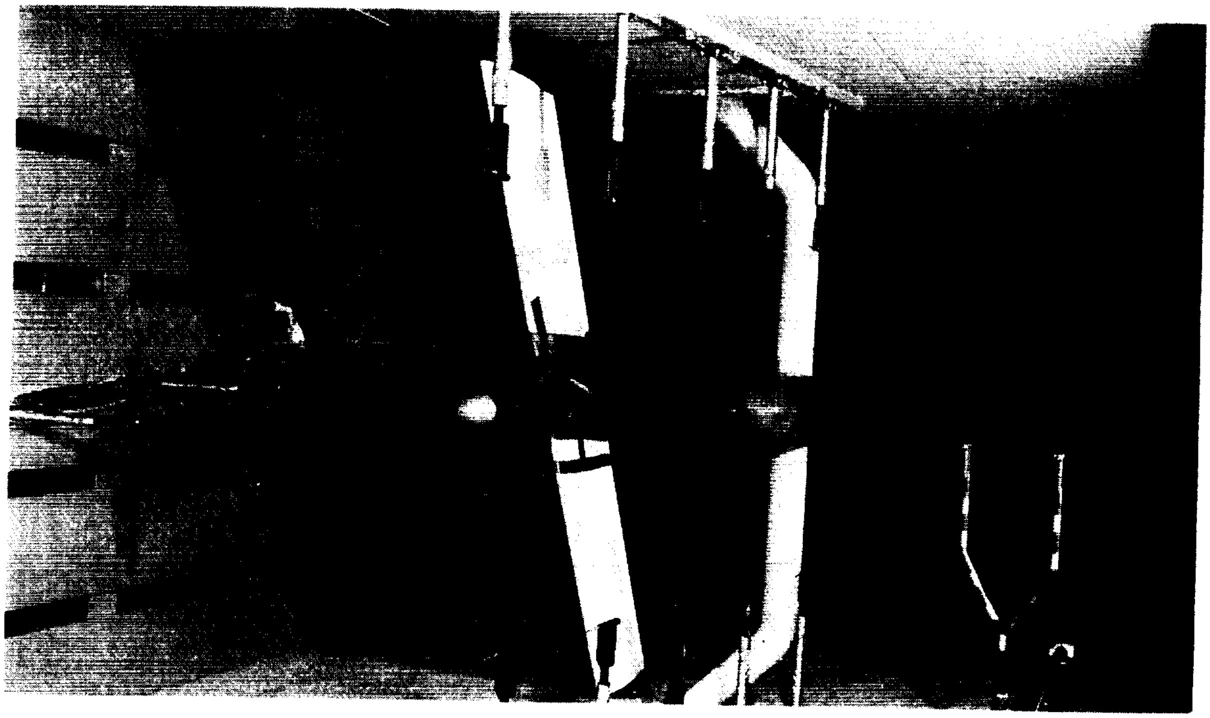

CD-87-29485

Figure 4. - SR-7A propeller model in 9- by 15-Foot Anechoic Wind Tunnel.

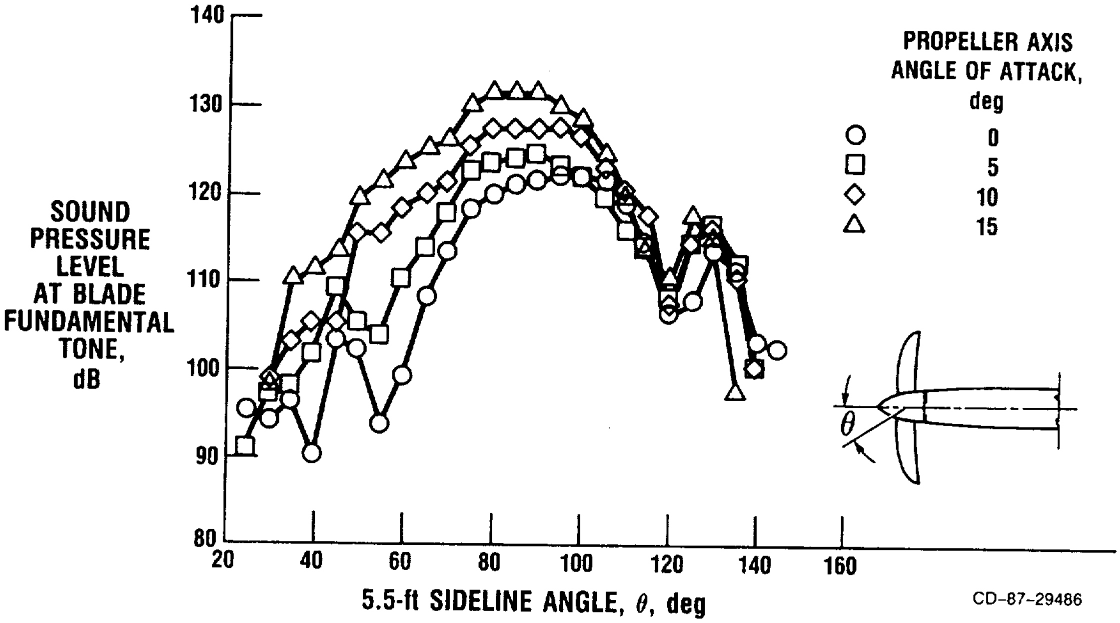

CD-87-29486

Figure 5. - Effect of angle of attack on flyover noise (single-rotation propeller SR-7A; 9- by 15-Foot Wind Tunnel; takeoff blade angle, 37.8°; tip speed, 800 ft/sec; tunnel Mach number, 0.2).

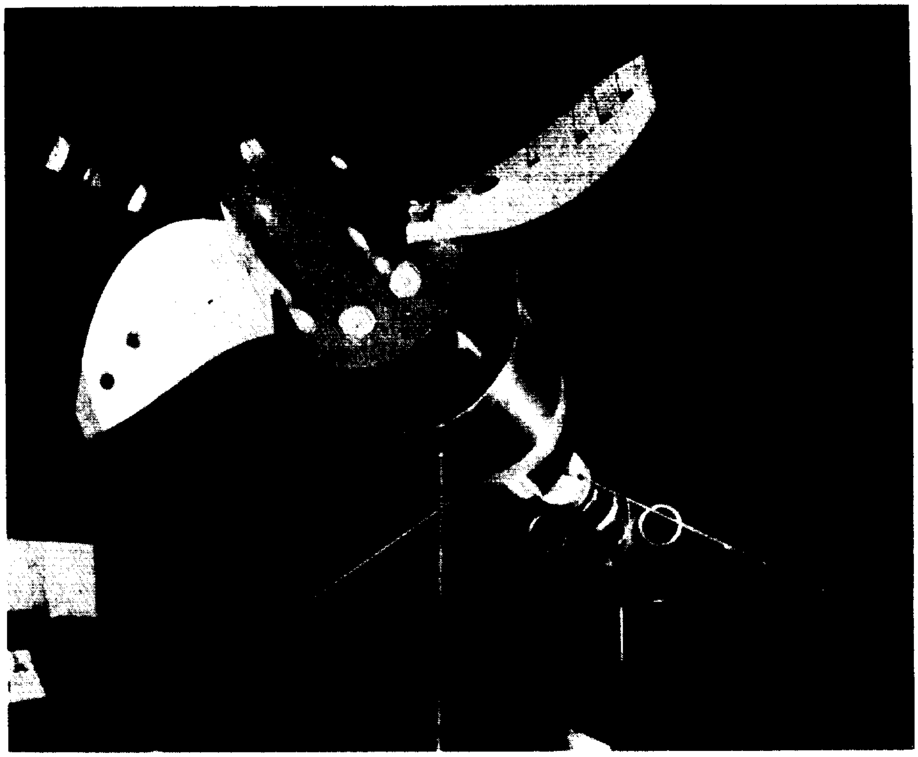

CD-87-29487

Figure 6. - Two-blade version of large-scale advanced propfan (LAP).

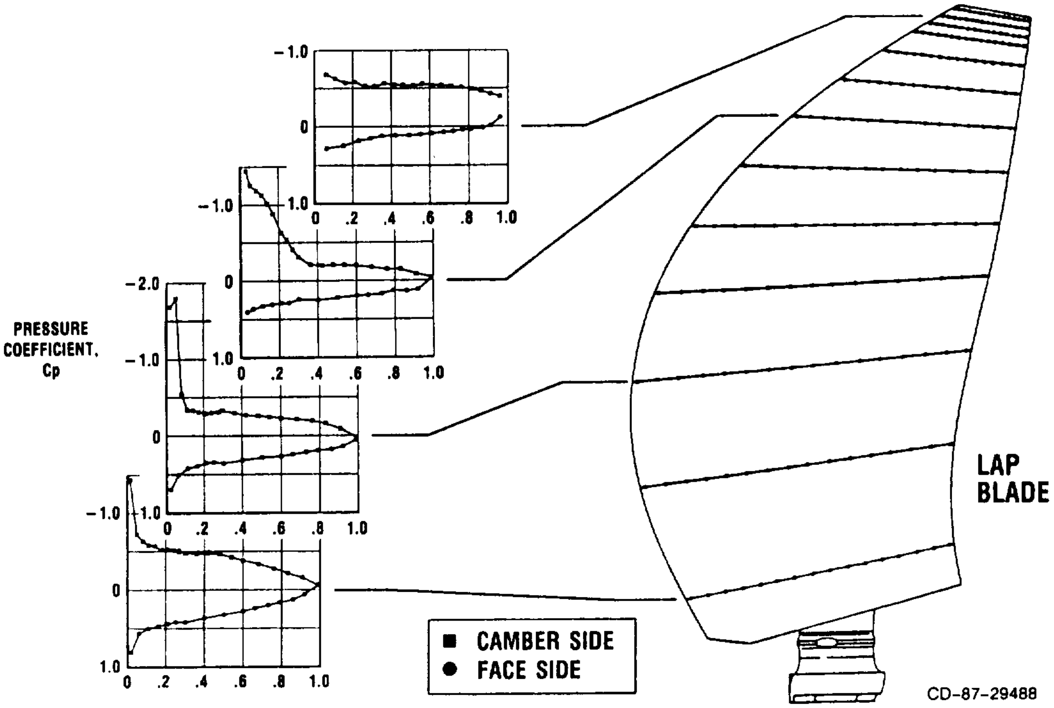

CD-87-29488

Figure 7. - Blade pressure measurements on full-scale propeller (low-speed conditions).

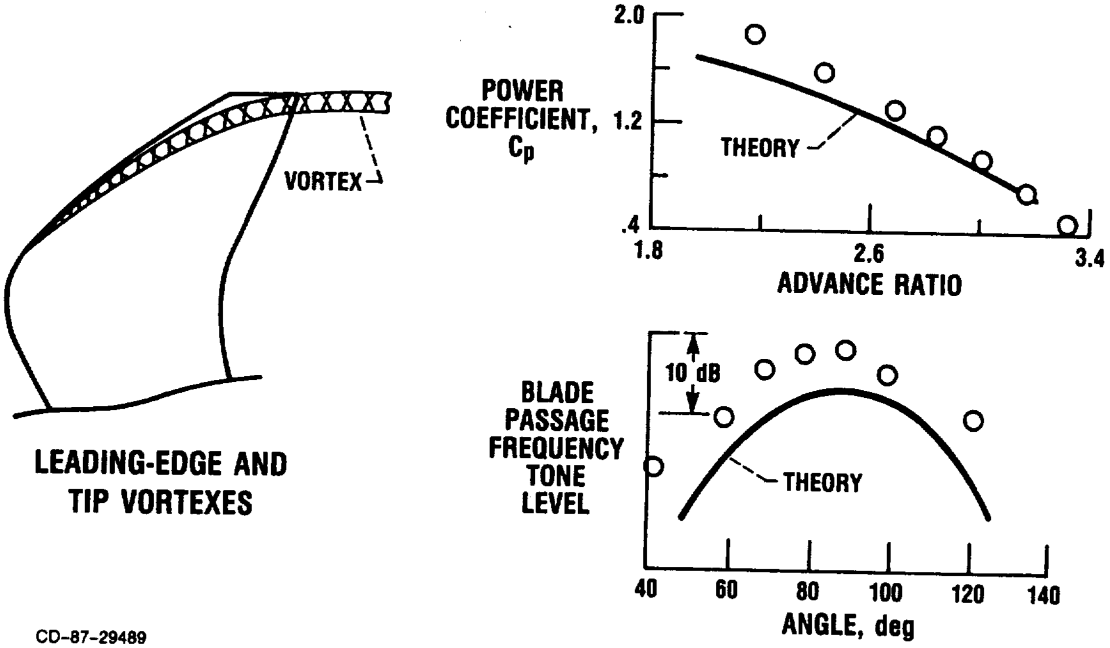

CD-87-29489

Figure 8. - Off-design operation.

CD-87-29490

Figure 9. - Visualization of propeller blade surface flow (off-design conditions).

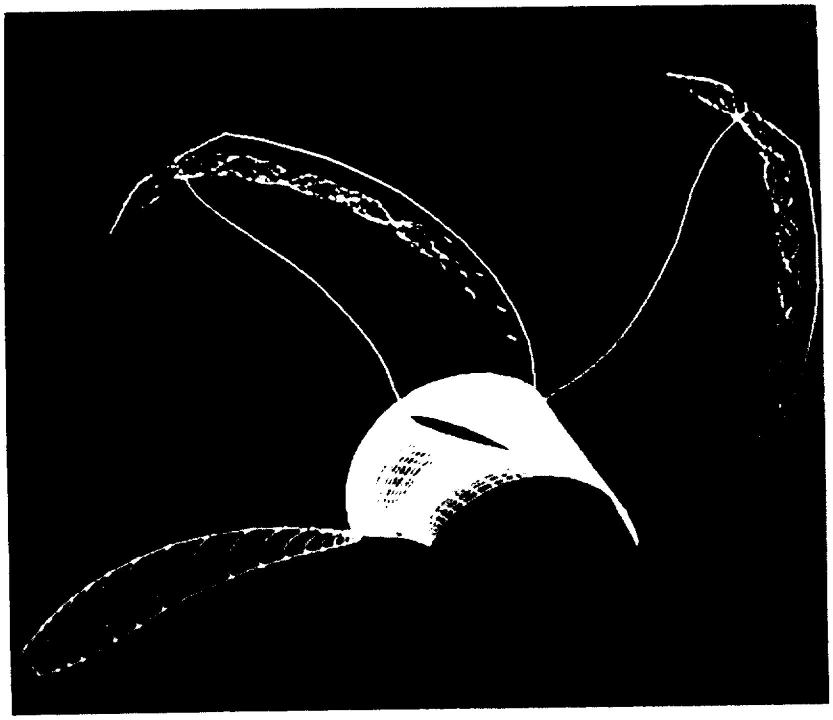

CD-87-29491

Figure 10. - Computed streamlines on CRP-X1 propeller (Mach 0.2; J = 1.0).

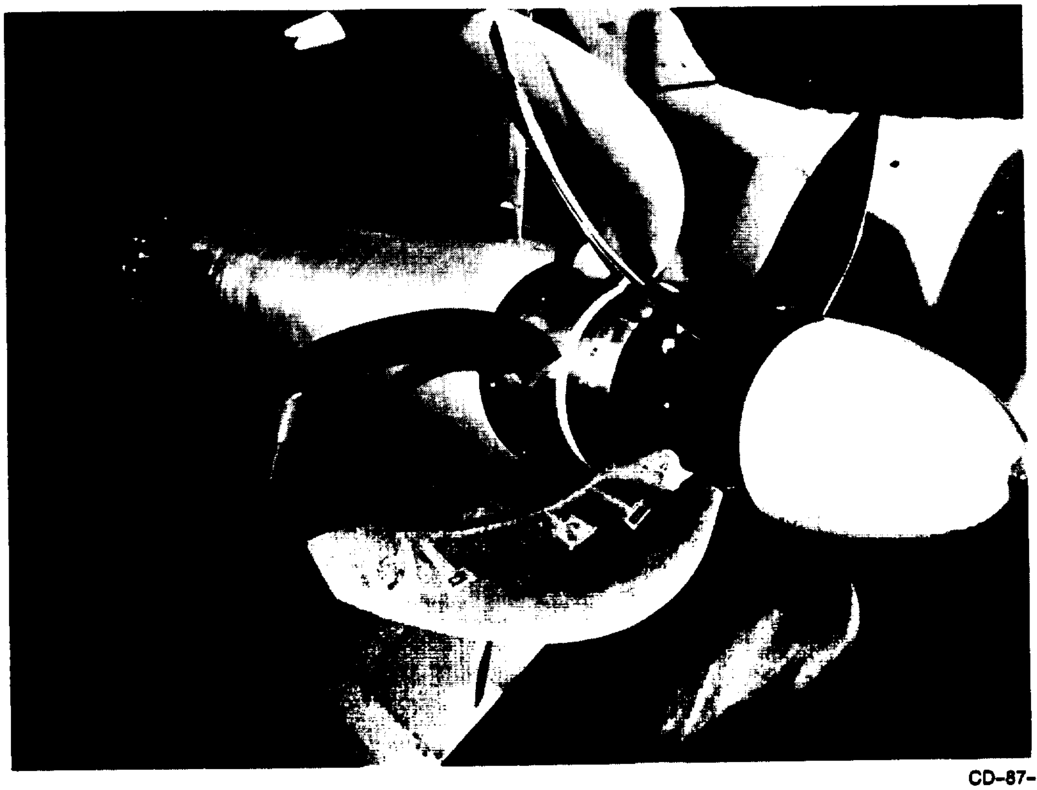

CD-87-29492

Figure 11. - Counterrotating propeller (CRP-X1) in UTRC wind tunnel.

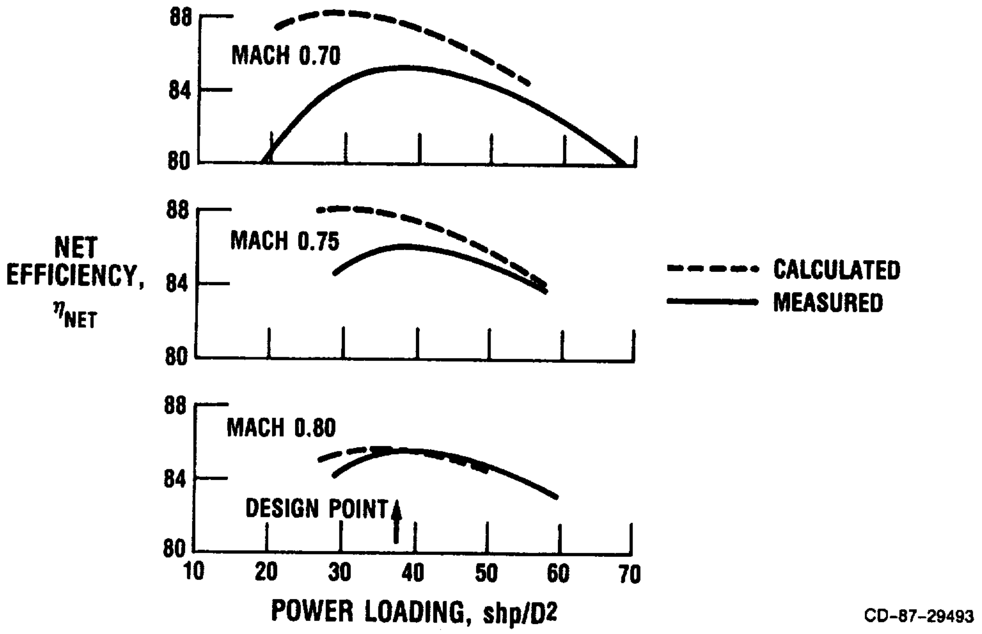

Figure 12. - CRP-X1 performance comparison ($\Delta\beta$ = 2.6; tip speed, 750 ft/sec).

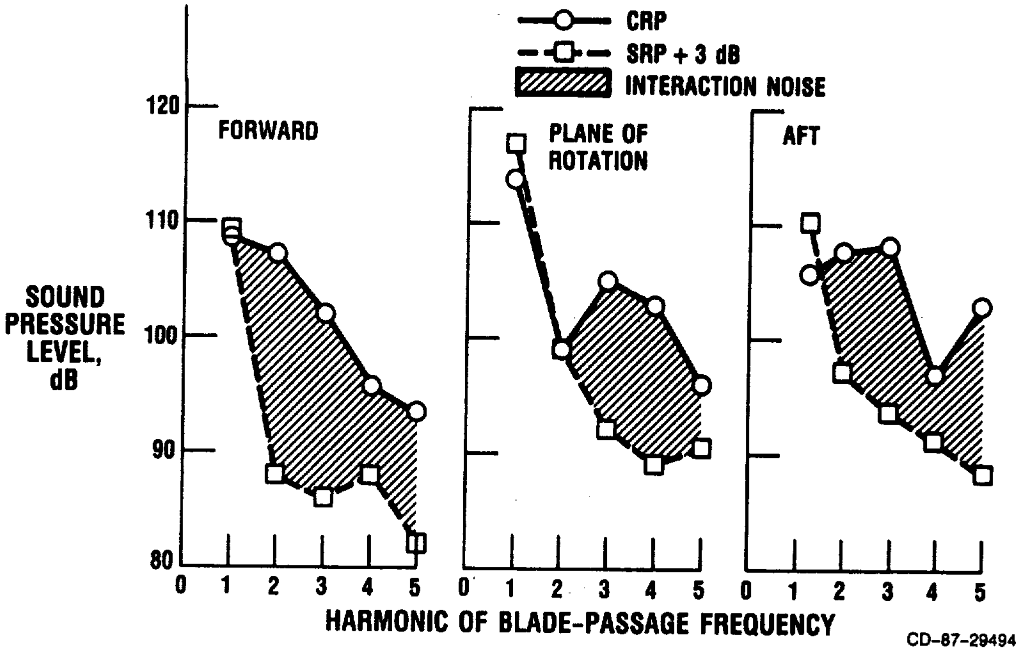

Figure 13. - Counterrotation propeller interaction noise (CRP-X1 at takeoff conditions: V_T = 650 ft/sec; 100 shp/rotor).

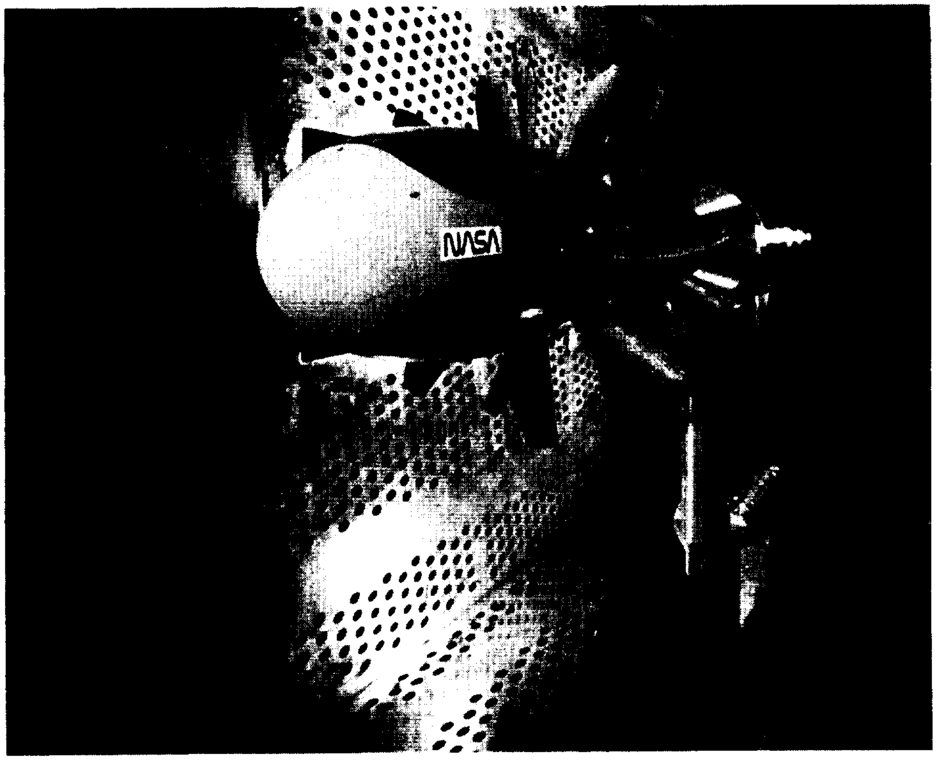

CD-87-29495

Figure 14. - Counterrotation propeller in Lewis 8- by 6-ft wind tunnel.

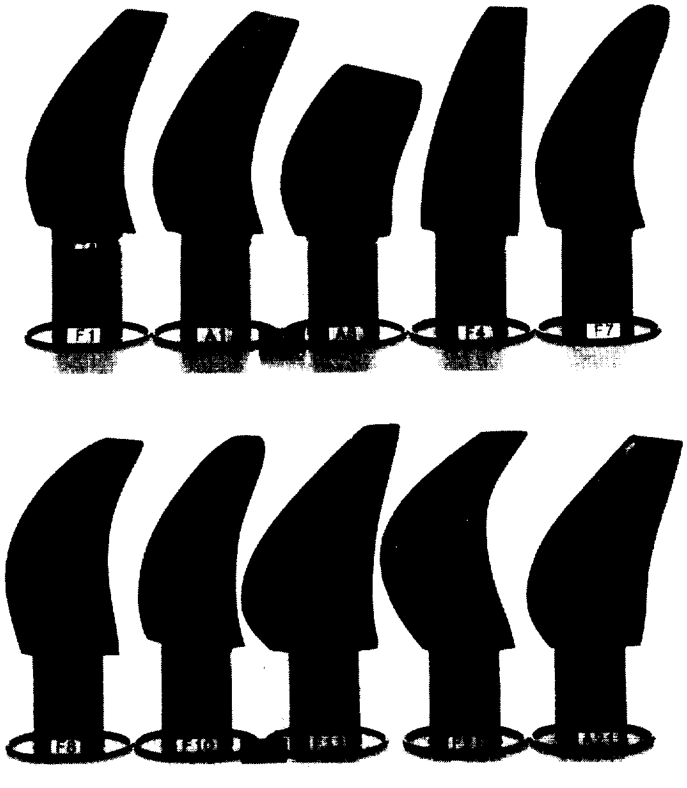

CD-87-29496

Figure 15. - Model counterrotation propeller blades.

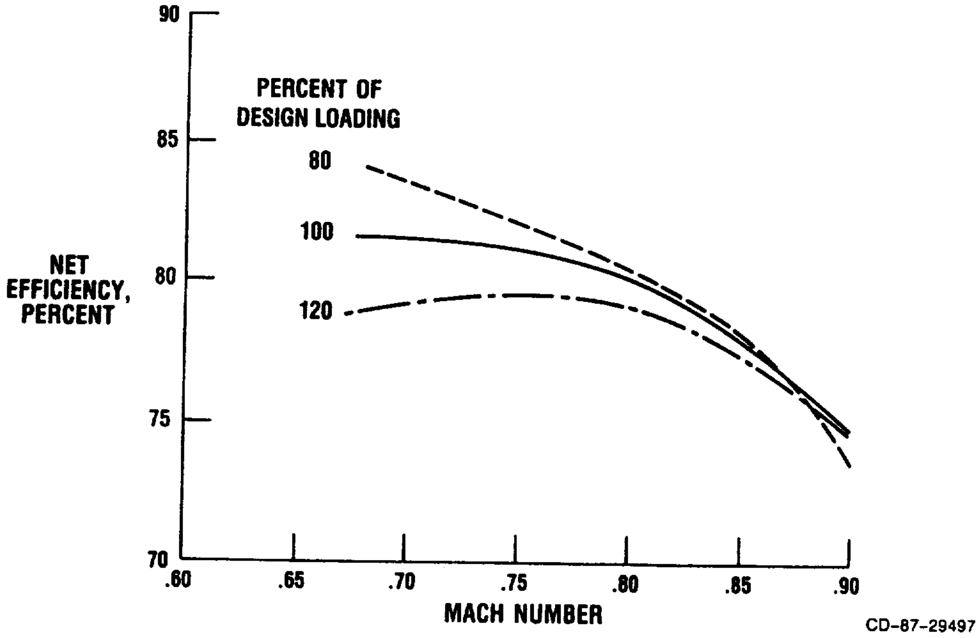

Figure 16. - F7-A7 performance summary (8+8 blade configuration; nominal spacing; matched speed; tip speed, 780 ft/sec).

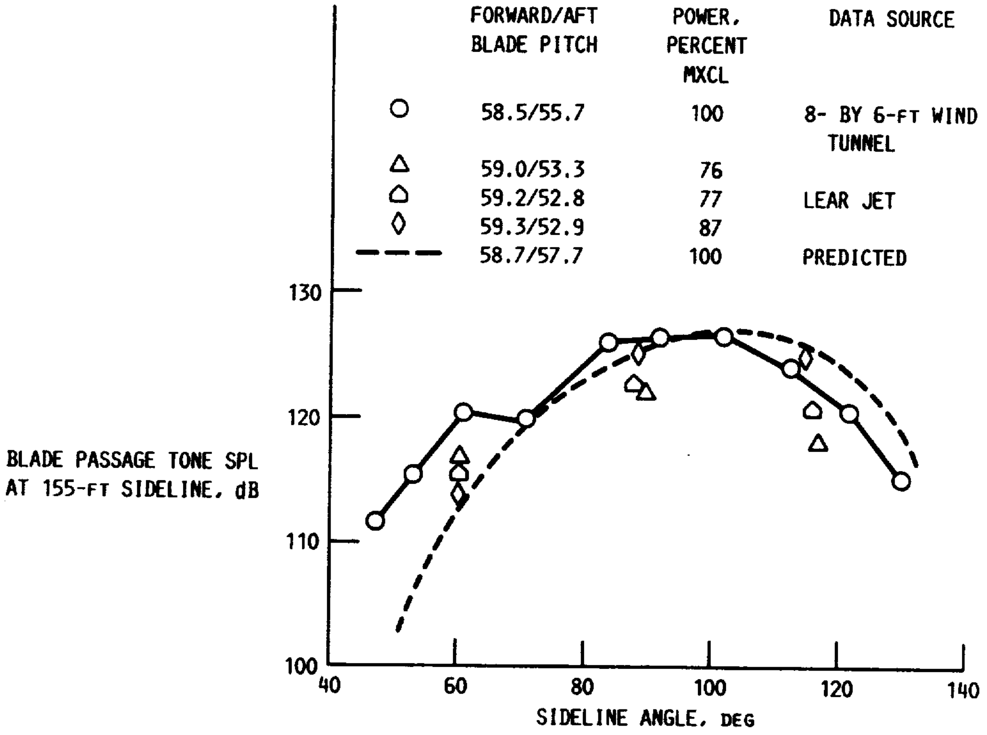

Figure 17. - Counterrotation tone levels at cruise (propeller F7-A7; Mach 0.72; altitude, 35 000 ft).

CD-87-29499

Figure 18. - Counterrotation model F7-A7 in Lewis 9- by 15-Foot Anechoic Wind Tunnel.

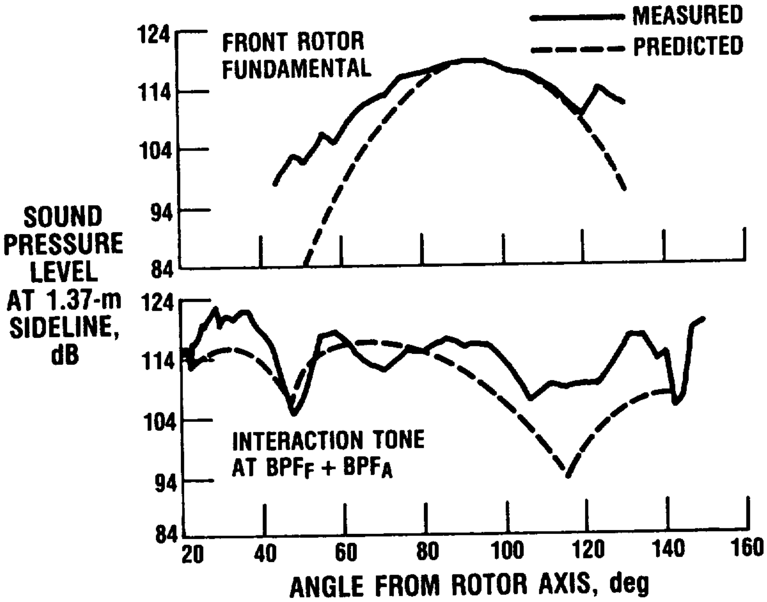

CD-87-29500

Figure 19. - Counterrotation propeller noise at takeoff (propeller F7-A7; Mach 0.2; 9- by 15-Foot Anechoic Wind Tunnel).

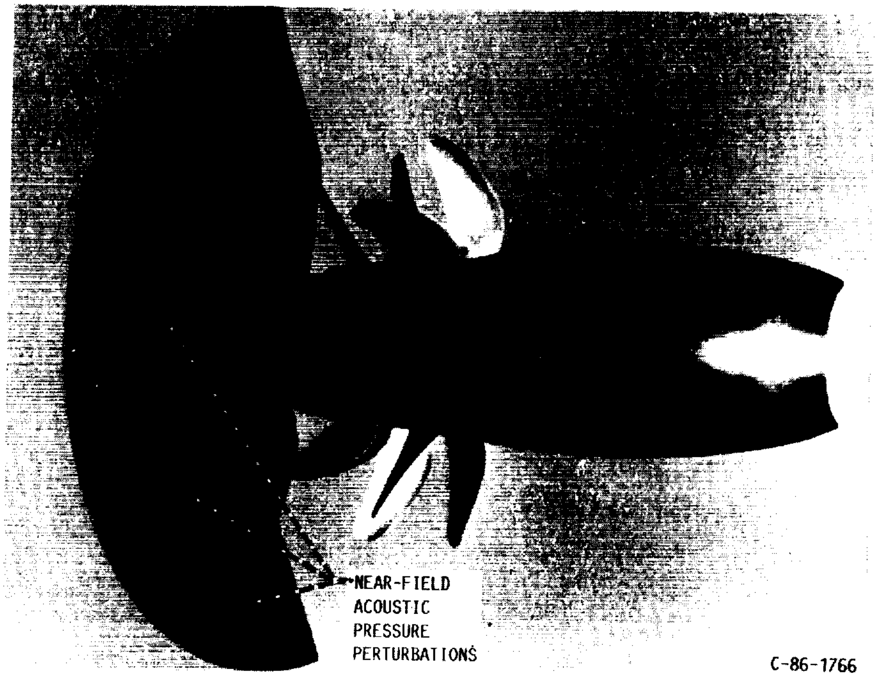

Figure 20. - Three-dimensional Euler analysis of counterrotation propeller flow field.

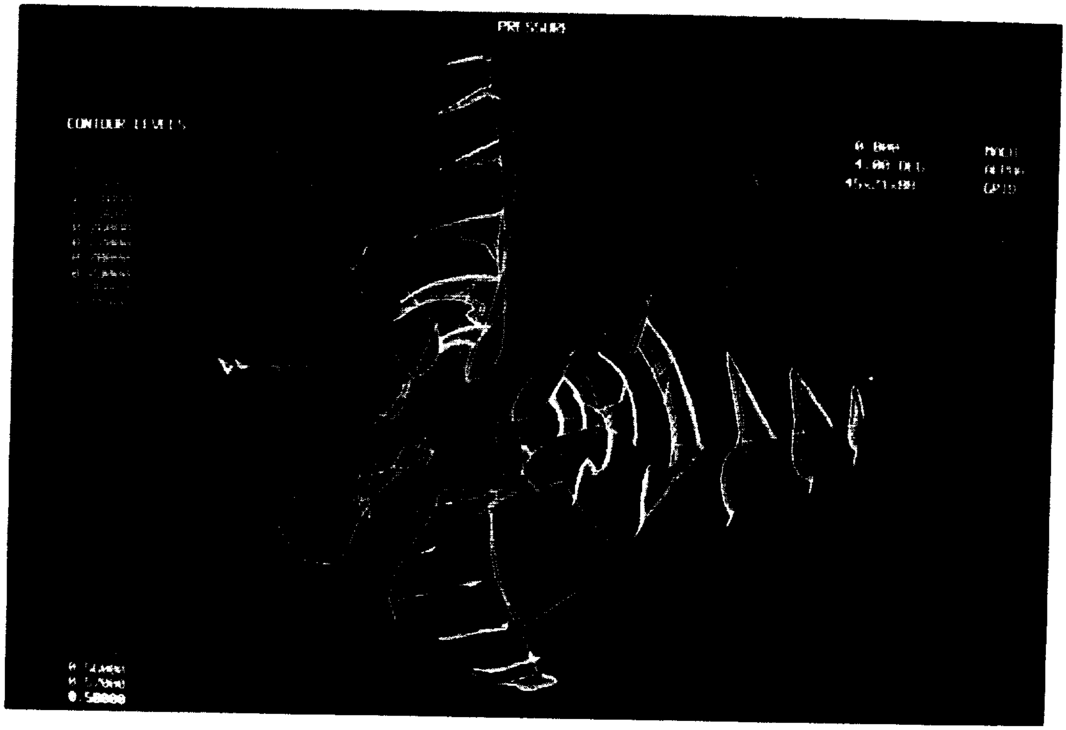

CD-87-29502

Figure 21. - Unsteady three-dimensional Euler code solution for propeller at angle of attack.

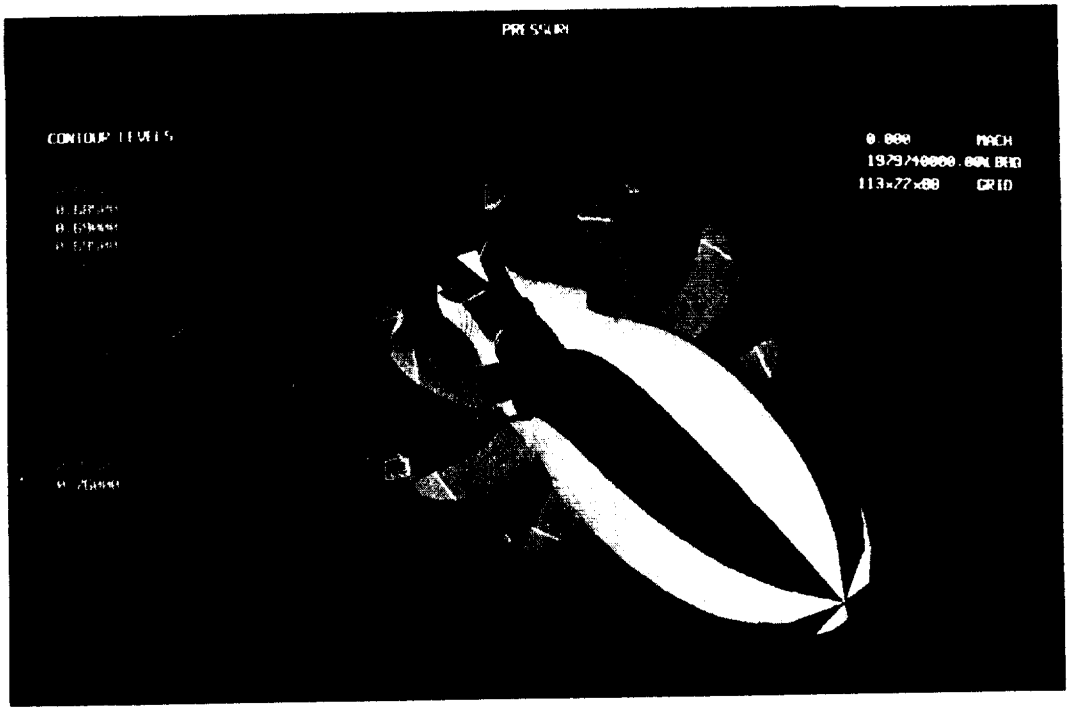

CD-87-29503

Figure 22. - Unsteady three-dimensional Euler solution for counterrotation propeller.

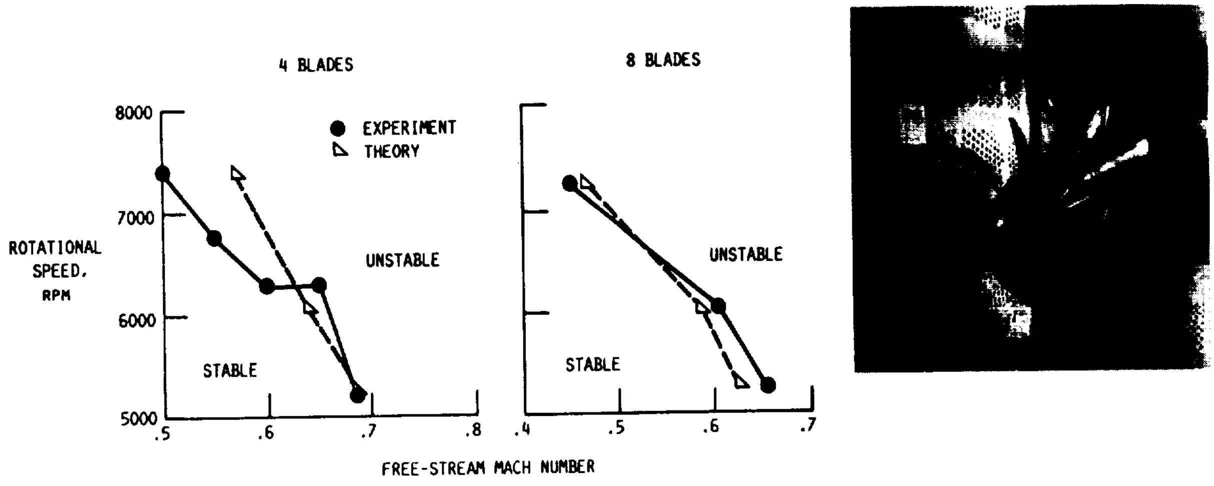

CD-87-29586

Figure 23. - Comparison of measured and calculated flutter boundaries (SR3C-X2 propfan model).

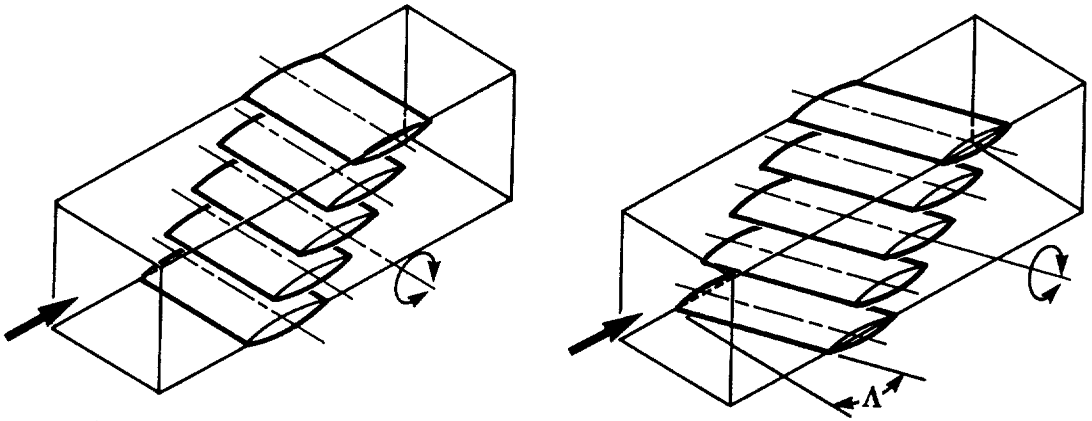

UNSWEPT CASCADE

SWEPT CASCADE

- **EXPERIMENT TO DETERMINE EFFECT OF BLADE SWEEP, Λ, ON TRANSONIC CASCADE AERODYNAMICS**
- **STEADY AND UNSTEADY BLADE SURFACE PRESSURES**
- **TORSIONAL BLADE OSCILLATION**
- **DATA USED TO BENCHMARK STEADY AND UNSTEADY ANALYSES**

CD-87-29505

Figure 24. - Swept cascade experiment.

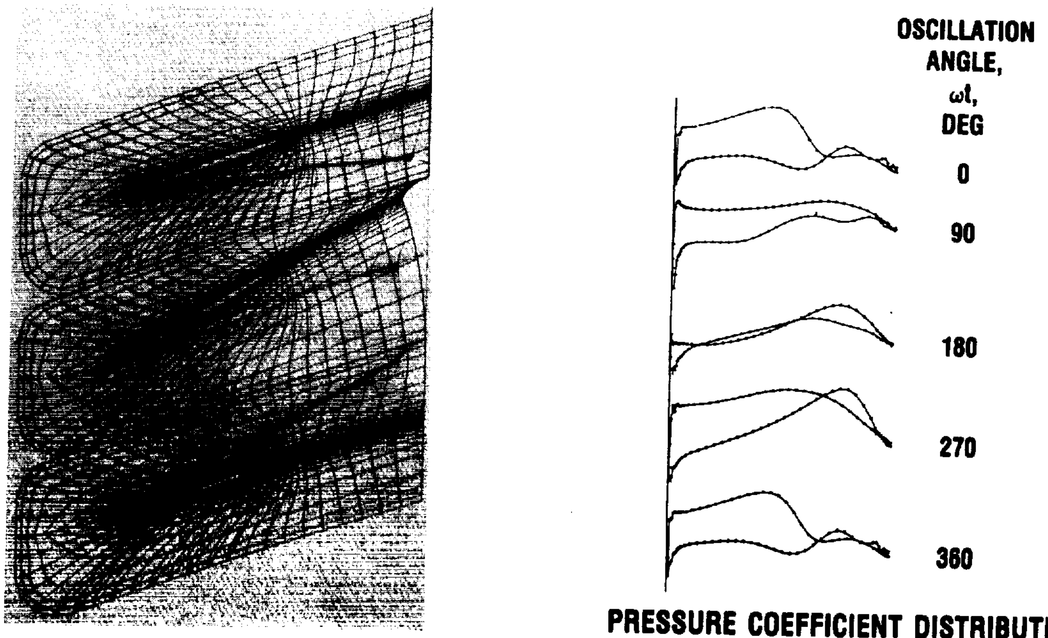

DEFORMING GRID (EXAGGERATED MOTION)

PRESSURE COEFFICIENT DISTRIBUTION (CENTER BLADE)

CD-87-29506

Figure 25. - Two-dimensional unsteady, Navier-Stokes, oscillating cascade analysis (NACA 16-004 cascade; $M_1 = 0.75$; $g = 1.0$; $\alpha_m = 21°$; $\alpha_1 = \pm 2.0°$; $k = 0.20$; $Re = 5.0\times10^6$; $\theta = 20°$; $\sigma = 90°$).

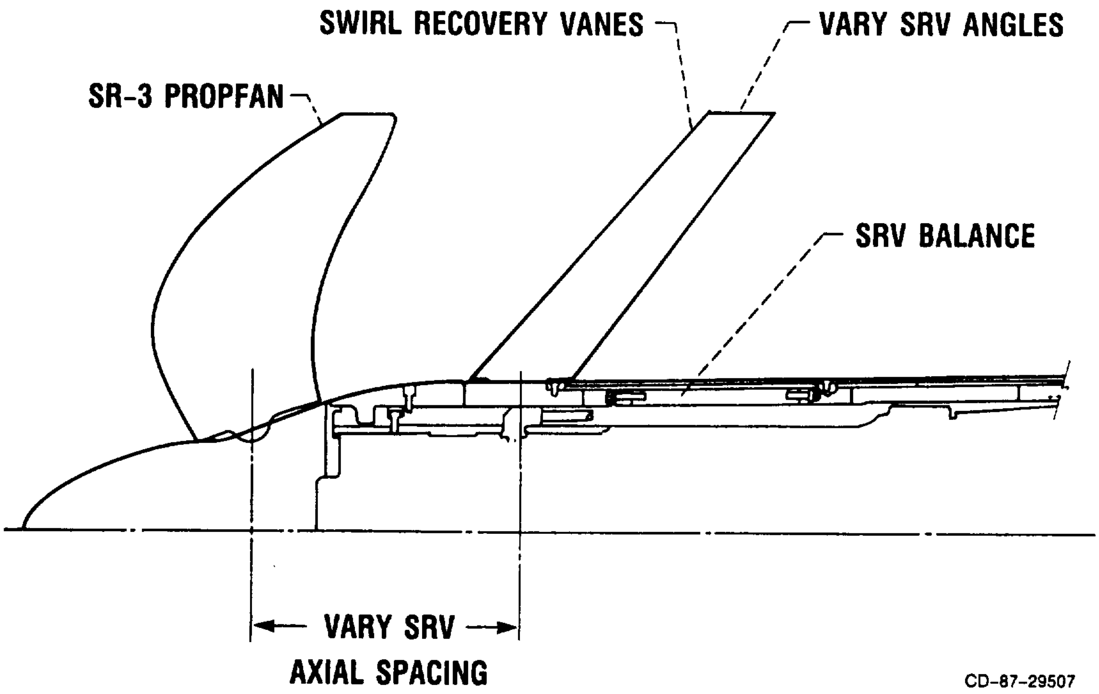

Figure 26. - Swirl recovery vane experiment.

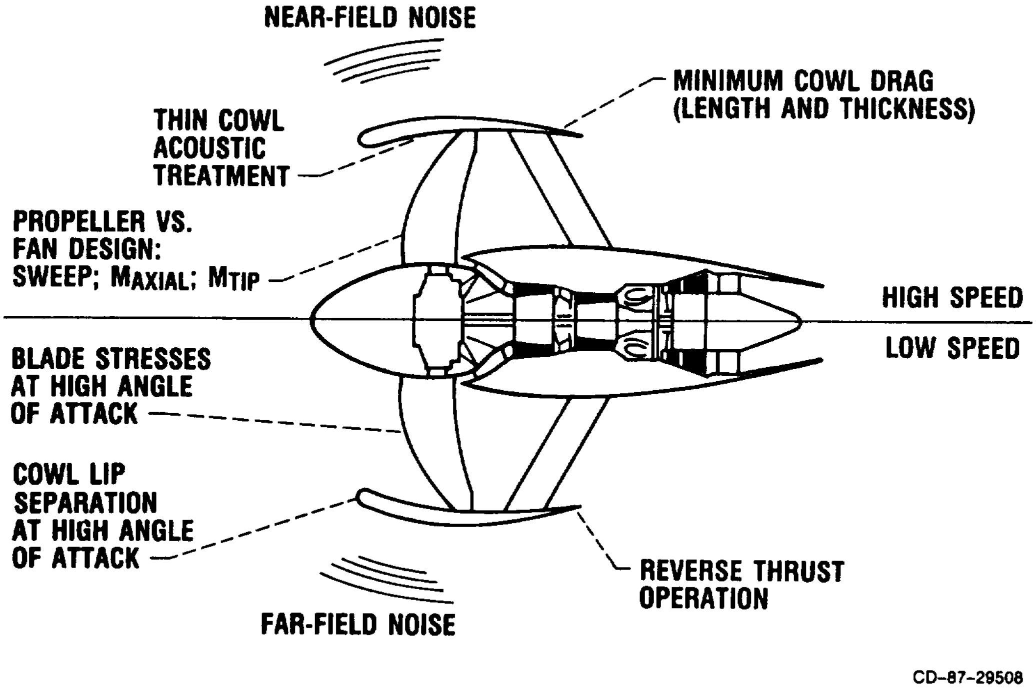

Figure 27. - High-speed ducted propeller issues.

	PRESENT	FUTURE
AERODYNAMICS	• 3D STEADY EULER CODES	• 3D UNSTEADY EULER & NAVIER-STOKES CODES
	• PERFORMANCE MEASUREMENT, PROBE SURVEYS, & BLADE PRESSURES	• DETAILED FLOW FIELD DIAGNOSTICS - LASER VELOCIMETER
		• ULTRA-HIGH BYPASS DUCTED PROPELLER PERFORMANCE
ACOUSTICS	• 3D CODES USING DETAILED STEADY AERO INPUT	• INTERACTION & INSTALLATION EFFECTS FROM DETAILED UNSTEADY AERO INPUT
	• CRUISE AND TAKEOFF SIGNATURES FOR SRP & CRP INSTALLATIONS	• DETAILED NOISE MAPS FOR INSTALLED CONFIGURATIONS
		• CODES & DATA FOR SHORT, THIN DUCTS
AEROELASTICS	• FLUTTER BOUNDARY MEASUREMENT & PREDICTION FOR SRP'S	• FLUTTER BOUNDARY MEASUREMENT & PREDICTION FOR CRP'S
	• FIRST GENERATION STRUCTURAL OPTIMIZATION CODES	• STALL FLUTTER & FORCED RESPONSE FOR SRP'S & CRP'S

CD-87-29509

Figure 28. - Propeller research areas of emphasis.